Modeling of CO_2 Gasification of Carbon for Integration with Solid Oxide Fuel Cells

Andrew C. Lee and Reginald E. Mitchell
Thermosciences Group, Mechanical Engineering Dept., Stanford University, Stanford, CA 94305

Turgut M. Gür
Dept. of Materials Science and Engineering, Stanford University, Stanford, CA 94305, and
Direct Carbon Technologies, LLC, Palo Alto, CA 94301

DOI 10.1002/aic.11713
Published online February 19, 2009 in Wiley InterScience (www.interscience.wiley.com).

This modeling study focuses on gasification of carbon by CO_2 in a minimally fluidized bed containing a solid oxide fuel cell (SOFC). Kinetic parameters for a five-step reaction mechanism characterizing the Boudouard reaction ($C + CO_2 \rightarrow 2CO$) were determined thermogravimetrically at 1 atm from 973 to 1273 K. Experimentally determined kinetic parameters are employed in a transport model that predicts velocities and gas concentration profiles established in the carbon bed as a consequence of convection, diffusion, and heterogeneous reaction. The model is used to simulate the effect of an imbedded SOFC, in contact with the carbon bed. Although the model does not assume particular I-V characteristics for the fuel cell, it indicates that current densities in the practical range of 100–1000 mA/cm^2 can be supported. Results show that temperature strongly affects the current density, whereas CO_2 flow rate has only a weak effect. *AIChE J,* 55: 983–992, 2009
Keywords: modeling, solid oxide fuel cell, gasification, carbon, Boudouard reaction

Introduction

Coal is the cheapest and most abundant of all fossil fuels. In 2004, about 6.1 billion short tons of coal were consumed in the world, which constituted about 26% of the total energy used.[1] Nearly one-third of the electric power consumed worldwide is derived from coal. It is used to generate over half of the electricity consumed in the United States, which has over 100 years of coal reserves.[2] Coal is projected to play a significant role in electric power generation in the United States for the foreseeable future. This is also true for China and India, two countries whose energy demands are increasing at rates never before experienced.

When electricity is produced from coal in present-day power generation plants, significant quantities of CO_2 are released into the atmosphere via the stack gases, which typically contain only about 15% CO_2 with the balance primarily nitrogen. More than one-third of the anthropogenic CO_2 atmospheric emissions come from coal. To keep atmospheric CO_2 concentrations below levels that can cause significant climate change, CO_2 must be removed from power-plant effluent streams using energy intensive and costly processes, and finally sequestered. To reduce the quantities of CO_2 that must be sequestered, it is necessary to increase the conversion efficiency from coal to electricity. To this end, we have embarked on a research effort to gain the understanding needed to develop a direct coal fuel cell (DCFC).[3,4] The electrochemical conversion of coal to electrical energy offers the possibility of achieving high conversion efficiencies. This is partly due to the high ceiling value of the theoretical

Correspondence concerning this article should be addressed to A. C. Lee at aclee@stanford.edu.

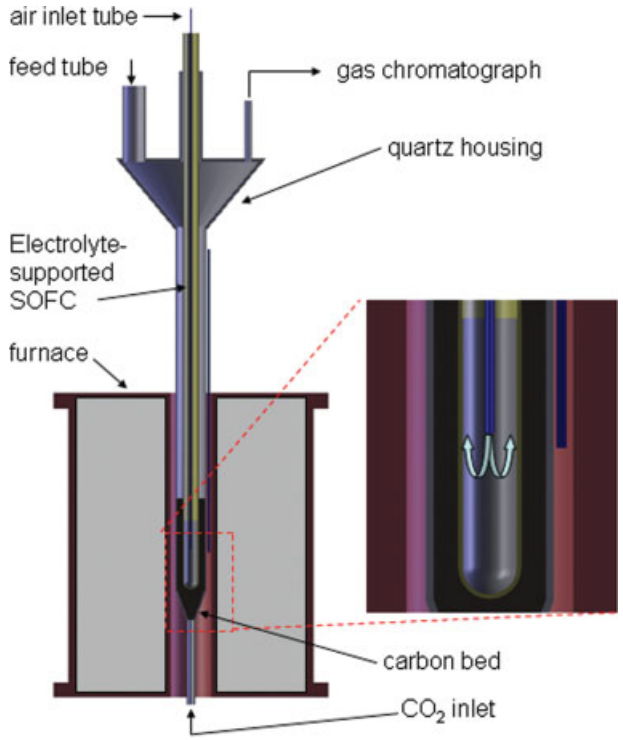

Figure 1. Schematic of the fluidized bed, direct carbon SOFC, illustrating a tubular configuration for the YSZ electrolyte membrane.

[Color figure can be viewed in the online issue, which is available at www.interscience.wiley.com.]

efficiency for electrochemical conversion of carbon to CO_2. Based on a preliminary thermodynamic analysis, the thermal efficiency for this DCFC approach is nominally 50%, and can be increased to nearly 60% with the addition of a steam bottoming cycle. This compares favorably with the nominal efficiency range of 30–45% reported for conventional and IGCC-type power plants.

In our approach, coal is gasified by flowing CO_2 inside a solid oxide fuel cell (SOFC) arrangement that contains a slightly agitated fluidized bed, yielding CO as a gasification product via the well-known Boudouard reaction: $C + CO_2 \rightarrow 2CO$. The CO reacts with oxygen at the triple-phase boundaries (TPBs) at the anode surface of the SOFC. The oxygen is supplied by selective transport through an oxide ion conducting solid electrolyte membrane. In our approach, we use yttria-stabilized zirconia (YSZ) as our electrolyte membrane.

A schematic of the experimental setup is shown in Figure 1, which illustrates a tubular configuration for the YSZ electrolyte membrane. The cathode of the fuel cell is coated onto the inner surface of the YSZ tube whereas the anode layer is coated onto the outside. Air is supplied to the inside of the tube at a flow rate sufficient to avoid oxygen depletion at the cathode compartment. The oxygen is transported by lattice diffusion through the YSZ membrane leaving behind the nitrogen. For this to happen, oxygen picks up electrons from the external circuit through the cathode and is reduced to oxide ions, which are then incorporated into the YSZ solid electrolyte at the TPBs and transported to the anode side of the tube. Using ionic notation, the electrochemical reduction of oxygen at the cathode is represented as follows:

$$\frac{1}{2}O_{2(g)} + 2e^-_{\text{electrode}} \rightarrow O^{-2}_{(YSZ)} \tag{1}$$

The oxide ions migrate under the influence of the chemical potential gradient through the YSZ solid electrolyte membrane from the cathode to the anode, where they participate in the electrochemical oxidation of CO.

$$CO(g) + O^{-2}_{(YSZ)} \rightarrow CO_{2(g)} + 2e^-_{(\text{electrode})} \tag{2}$$

The electrons that are released during the oxidation reaction at the anode travel through the external circuit towards the cathode, producing useful electricity. The chemical potential difference of oxygen across the solid oxide electrolyte, between the cathode and anode, is a measure of the cell potential that provides the driving force for oxide ion transport. Under equilibrium conditions at 1 atm total pressure, it is equal to the open circuit potential, given by the Nernst equation:

$$E = -\frac{\Delta G^0_{CO+0.5O_2\rightarrow CO_2}}{nF} - \frac{RT}{nF}\ln\left(\frac{P_{CO_2,a}}{P_{CO,a}P^{0.5}_{O_2,c}}\right)$$

$$= -\frac{RT}{nF}\ln\left(\frac{P^{0.5}_{o_2,a}}{P^{0.5}_{o_2,c}}\right) \tag{3}$$

Here, E is the equilibrium potential of the fuel cell under open circuit conditions, ΔG^0 is the Gibbs free energy of reaction at temperature T and reference pressure of 1 atm with unit activities, R is the gas constant, F is Faraday's constant, and n is the number of electrons transferred per oxygen atom ($n = 2$). The CO_2, CO, and O_2 partial pressures at the anode are denoted by $P_{CO_2,a}$ $P_{CO,a}$, and $P_{O_2,a}$, respectively, whereas $P_{O_2,c}$ denotes the oxygen partial pressure at the cathode. In our system, the oxygen partial pressure at the cathode is fixed at 0.21 atm, the partial pressure of oxygen in air, and the partial pressure at the anode under open circuit conditions is determined by the half cell equilibrium at the anodic surface. For direct carbon oxidation, nearly 1.0 volt of open circuit voltage is expected at 1173k whereas CO oxidation would produce nominally 0.85 volts, depending on the CO/CO_2 ratio.

In this article, we present our efforts, to date, to develop a model of the direct carbon fuel cell operating on CO produced from CO_2 gasification of carbon. The experimental activities undertaken to determine the kinetic parameters that describe carbon reactivity to CO_2 are discussed and the equations used to describe the effects of mass transport and chemical reaction in the coal bed are presented. In this preliminary treatment, focus is on the effects of mass transport and kinetics-limited chemical reaction in the bed of particles. Comparisons are presented between predicted results and experimental observations for validation of the carbon bed processes. The model is then used to simulate the impact of current density, system temperature, and gas flow rate on performance of the DCFC when a tubular anode is

imbedded. The model presented here does not resolve the I-V characteristics of the fuel cell, but rather specifies a current flux at the bed-anode boundary. The net CO and CO_2 fluxes at this boundary are then fixed by the prescribed current density. The resulting gas concentration profiles under varying current densities will give a fundamental measure of how much current the gasification-driven DCFC can support.

Background

Carbon-based fuel cells

There have been many attempts to consume carbon directly in a fuel cell since the early work of Becquerel[5] in 1855, who used a carbon rod as the anode and platinum as the oxygen electrode in a fuel cell that employed molten potassium nitrate as the electrolyte. When oxygen was blown onto the platinum electrode, a current was observed in the external circuit. The lifetime of the cell was limited due to the direct chemical oxidation of carbon by the potassium nitrate electrolyte. Jacques,[6] in the late 1800's, successfully operated a molten sodium hydroxide electrolyte cell contained in an iron pot that served as the air cathode and a carbon rod, as the consumable anode.

Following the work of Weaver et al.,[7] there has been renewed interest in employing molten salts or molten metals to convert carbon in a fuel cell. In these efforts, fine particles of carbon (or coal) were dispersed in the molten medium in excess of the percolation limit so as to make a network of particle-to-particle contacts that carry the electrons needed for the reaction and serve as an extended anode. In molten salt systems that employ molten carbonate[7,8] and molten hydroxide electrolytes,[9] oxygen is supplied to the carbon particle in the form of a carbonate ion (CO_3^{-2}) or a hydroxide ion (OH^-), respectively, whereas in the case of model studies for molten metal anodes,[10,11] oxygen is envisioned to be supplied to carbon in the form of a metal oxide, which on reaction with carbon is reduced back to metal. These molten anode fuel cells operate in the 400–1500°C temperature range depending on the molten system employed.

The operating principle of DCFC system presented here is significantly different from these molten anode fuel cell systems. It is a gas-solid system and hence, is expected to be capable of providing higher power densities than is possible in molten systems due to the higher mass transport and chemical reaction rates. Also, it may potentially be less complicated to operate. In addition, it is easier to understand and model the reactions at the gas-solid interfaces. Benefits also exist with respect to ease of ash removal from the carbon (coal) bed in a gas-solid system.

Our approach stems from an earlier proof-of-concept study in which the direct conversion of carbon inside a fuel cell was demonstrated successfully.[12] This preliminary study utilized a fixed carbon bed in a SOFC that employed a stabilized zirconia tube. The configuration was capable of drawing currents in excess of 30 mA/cm^2. More recently, we have demonstrated a CO_2 fluidized bed direct carbon fuel cell where, carbon, coal, and biomass were converted successfully into electricity in a single process step.[3,4]

The C—CO_2 reaction system

Our approach relies on the in situ production of CO inside the fuel cell via reactions between carbon and carbon dioxide. The C—CO_2 reaction system has received considerable attention over the years and in this study, we use the reaction mechanism put forth by Ma,[13] who developed a mechanism capable of describing the results of several previous investigations, in particular, the early atmospheric carbon—CO_2 studies of Ergun,[14] the high-pressure char gasification studies of Blackwood and Ingeme,[15] the CO inhibition studies of Koenig et al.,[16] and the high pressure, high-CO char gasification studies of Tsai.[17]

The mechanism employed in this study is presented in Table 1. In the reactions, C_f denotes a free carbon site (i.e., a carbon site available for adsorption); C(O) and C(CO) denote an adsorbed oxygen atom and an adsorbed CO molecule, respectively; and C_b denotes a bulk carbon site (an underlying site that will be exposed on desorption of a carbon atom from the carbonaceous matrix). Bulk carbons are assumed to have unit activity when determining reaction rates. To account for the variations in the chemical properties of adsorbed oxide complexes due to the local microscopic irregularities of char surfaces,[18–22] a distribution of desorption energies is used when determining the rate of the desorption reaction (R.2).

The reaction mechanism yields the following expression for the intrinsic char reactivity $R_{i,C}$, the net rate of removal of carbon atoms from the bulk char (in g/m^{2*} s):

$$R_{i,C} = \hat{M}_C\left(\hat{R}\hat{R}_2 + \hat{R}\hat{R}_3 - \hat{R}\hat{R}_4\right) \tag{4}$$

Here, $\hat{M}_c$ is the molecular weight of carbon and $\hat{R}\hat{R}_i$ is the net molar reaction rate for reaction i (in mol/m^2 s), which depends on the reaction rate coefficient of the reaction and the concentrations of the species involved. In our approach, the concentration of a gas-phase species is expressed in moles per unit volume (mol/m^3) and the concentration of an adsorbed surface species is expressed in moles per unit surface area (mol/m^2). The conversion rate of the char satisfies the following differential equation, which when integrated yields char conversion, x_C, as a function of time:

$$-\frac{1}{m_C}\frac{dm_C}{dt} = \frac{1}{(1-x_C)}\frac{dx_C}{dt} = S_{gC}R_{i,C} \tag{5}$$

The specific surface area of the char, S_{gC} (m^2/g), as a function of char conversion is derived from the results of Bhatia and Perlmutter[23]:

$$S_{gC} = S_{gC,0}\sqrt{1-\psi\ln(1-x_c)} \tag{6}$$

Table 1. Reduced Heterogeneous Reaction Mechanism for Char Reactivity to CO_2

$CO_2 + C_f \underset{k_{1b}}{\overset{k_{1f}}{\rightleftarrows}} CO + C(O)$	(R.1)
$C_b + C(O) \xrightarrow{k_2} CO + C_f$	(R.2)
$C_b + CO_2 + C(O) \xrightarrow{k_3} 2CO + C(O)$	(R.3)
$C_f + CO \underset{k_{4r}}{\overset{k_{4f}}{\rightleftarrows}} C(CO)$	(R.4)
$CO + C(CO) \xrightarrow{k_5} CO_2 + 2C_f$	(R.5)

This specific surface area model is based on the random pore model for describing gasification rates of porous materials and accounts for the variations in surface area that occur when closed-off pores open and when pores merge and coalescence as solid material is gasified. The higher the value of the structural parameter, ψ, the greater the microporosity of the char. The structural parameter can be estimated from true density and pore size distribution data but in the work presented in this article, we determine, via a least squares procedure, a value that best correlates the measured surface areas.

The production of CO and CO_2 due to the chemical reactions presented in Table 1 are given by

$$\hat{R}_{CO} = \hat{R}\hat{R}_1 + \hat{R}\hat{R}_2 + 2\hat{R}\hat{R}_3 - \hat{R}\hat{R}_4 - \hat{R}\hat{R}_5 \tag{7}$$

and

$$\hat{R}_{CO_2} = -\hat{R}\hat{R}_1 - \hat{R}\hat{R}_3 + \hat{R}\hat{R}_5 \tag{8}$$

These equations define the overall CO and CO_2 reaction rates, $\hat{R}_{CO}$ and $\hat{R}_{CO_2}$, respectively (in mol/m^{2*}s).

The changes in the adsorbed O and CO concentrations with time are governed by the following relations:

$$\frac{d[C(O)]}{dt} = \hat{R}\hat{R}_1 - \hat{R}\hat{R}_2 + [C(O)]S_{gC}R_{i,C}\left[1 - 0.5\psi(S_{gC,0}/S_{gC})^2\right] \tag{9}$$

$$\frac{d[C(CO)]}{dt} = \hat{R}\hat{R}_4 - \hat{R}\hat{R}_5 + [C(CO)]S_{gC}R_{i,C}\left[1 - 0.5\psi(S_{gC,0}/S_{gC})^2\right] \tag{10}$$

The last term on the right-hand-sides of Eqs. 9 and 10 account for the change in the adsorbed species concentration due to change in specific surface area. Previous results[24,25] have indicated that this contribution is relatively small, having the most impact early in conversion when new surface area is being exposed (giving adsorbed complexes more overall surface area to populate) and late in conversion when surface area is decreasing (giving oxide complexes less overall surface area to populate).

Given Arrhenius parameters, temperature, total pressure, and initial CO and CO_2 gas-phase concentrations, Eqs. 5 and 7–10 can be integrated simultaneously, along with Eqs. 4 and 6, to yield the extent of char conversion, the CO and CO_2 gas-phase mole fractions, and the adsorbed O-atom and CO surface concentrations as functions of time. The results would be valid for cases in which the char is totally penetrated by CO_2, which would be the case under kinetics-controlled gasification conditions. Such conditions exist at low gasification temperatures, for temperatures less than 1273 K.

Table 2. Activated Carbon Properties (Ultimate Analysis in wt %)

	As rec'd	Dry
Moisture	14.65	0.00
Carbon	80.56	94.39
Hydrogen	0.46	0.54
Nitrogen	0.30	0.35
Sulfur	0.11	0.13
Ash	2.59	3.03
Oxygen*	1.33	1.56
MAF MJ/kg (HHV)	32.4	

*by difference.

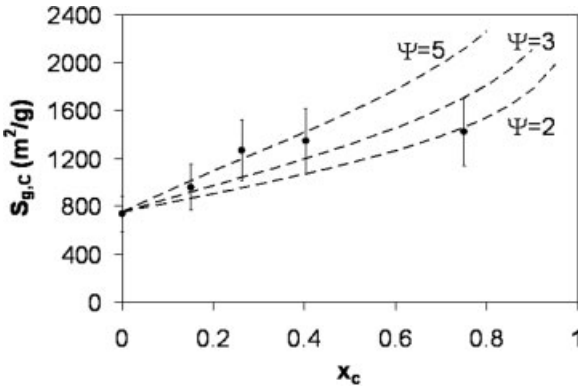

Figure 2. Specific surface area evolution for the coconut char.

The lines were calculated via Eq. 6 with $S_{gC,0}$ = 750 m^2/g and ψ values of 5, 3, and 2.

Experimental Procedures

Char reactivity to CO_2

Experiments were undertaken to determine the kinetic parameters that describe the gasification rate of the activated carbon. Specific surface area measurements were made so that the structural parameter in the surface area model could be determined. Temperature programmed desorption (TPD) tests were performed so that the parameters that describe the distribution in desorption energies of surface oxide complexes could be established, and gasification tests in CO_2-containing environments at selected temperatures were performed so that char conversion rate data could be obtained. These experiments were performed in a pressurized thermogravimetric analyzer (PTGA), an instrument that measures and records the weight changes of a sample placed in the balance pan in a chamber where the gas temperature, pressure and composition can be controlled. Our PTGA also permits the CO, CO_2, and O_2 concentrations in the gases exiting the chamber to be monitored. The details of the experimental procedures are described elsewhere,[13,24] and are only briefly described below.

An activated carbon derived from coconut char was used in this study (see Table 2). Samples of the activated carbon were subjected to gas adsorption tests in the PTGA to determine BET-surface areas via analysis of the adsorption data. Carbon dioxide was used as the adsorption gas in tests that were performed at 298 K and 10 atm using various mixtures of CO_2 in nitrogen. The slope and intercept of the BET-plots yielded the information to determine the specific surface area of the char sample, employing a value of 22.2 Å^2 for the molecular cross-section of CO_2.[26] Specific surface areas were measured during the course of certain gasification tests, yielding surface areas as a function of conversion. The data were correlated according to Eq. 6, yielding a value of 3 for the structural parameter of the char, as shown in Figure 2. Each error bar represents 20% uncertainty in the measured

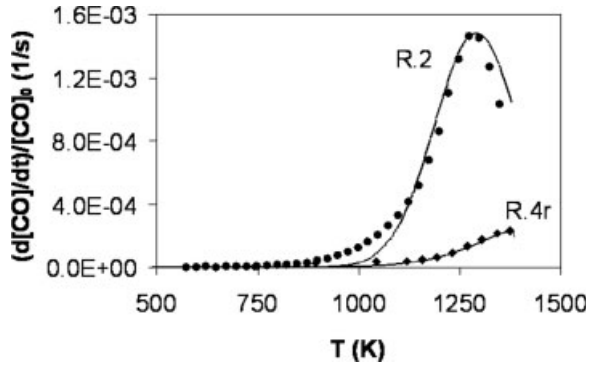

Figure 3. CO evolution rates measured (symbols) during TPD tests for R.2 and R.4r, along with predictions (lines) using a Gaussian distribution function.

value, the uncertainty determined in previous experiments employing a variety of coal and synthetic chars.[13,17,24]

In the TPD tests, the char sample placed in the balance pan of the PTGA is heated in nitrogen to 1373 K to drive off already-adsorbed oxide complexes, and then exposed to 100% CO_2 at 873 K for 30 min before being cooled to 300 K. During this time, oxygen was adsorbed onto the char surface. Once at 300 K, the gas in the PTGA chamber was switched to nitrogen and the sample was heated at a rate of 25 K/min. As the temperature increased, surface oxides desorbed from the carbonaceous material as carbon oxides. The mole fractions of CO and CO_2 measured in the PTGA exhaust yielded the distributions of desorption energies of adsorbed oxygen complexes, from which kinetic parameters for reaction R.2 were determined. With the coconut-based char used in this study, CO was the only oxide of carbon desorbed; no CO_2 was detected.

The distribution of the energies of adsorbed CO complexes on the char surface was measured in a similar manner. In these TPD tests, after cleaning the char sample in nitrogen, the sample was cooled to 300 K and exposed to 100% CO, then heated to 873 K at a rate of 25 K/min and held at 873 K for 30 min before cooling back to 300 K and switching to nitrogen to start another 25 K/min heating ramp. During the initial heating ramp to 873 K in carbon monoxide, CO was adsorbed onto the carbonaceous surface. Transient analysis of this data yielded the Arrhenius parameters, A_{4f} and E_{4f}, where A_i and E_i denote the pre-exponential factor and activation energy, respectively, for reaction i. [The subscript f denotes the forward direction of reaction i, the subscript r denotes the reverse direction.] During the second heating ramp in nitrogen, CO desorbed from the material. Mole fraction measurements yielded the distribution of desorption energies of adsorbed CO, from which kinetics parameters for reaction R.4r were determined.

In Figure 3, the measured desorbed-CO distributions along with the Gaussian distributions used to fit the data are shown. The fits yield a mean value of the activation energy for reaction (R.2) of 375 kJ/mol, with a standard deviation of 28 kJ/mol, and a mean value of the activation energy for reaction (R.4r) of 455 kJ/mol, with a standard deviation of 53 kJ/mol. The mean values of the activation energies are within expected ranges. The effective reaction rate coefficients for reactions (R.2) and (R.4r) are determined from Eq. 11, where ψ is the Gaussian distribution function having a mean activation energy $\bar{E}$ and a standard deviation σ.

$$k_{i,\text{eff}} = A_i \int_0^{E_{\max}} \underline{\Psi}\,(E, \bar{E}_i, \sigma_i) \exp(-E/RT) dE \qquad (11)$$

In the gasification tests designed to determine char reactivity to CO_2, a known weight of char was placed in the PTGA balance pan. Nitrogen was then admitted into the PTGA chamber and the temperature was increased to 1373 K at a heating rate of 25 K/min and held at this temperature for 30 min before cooling back to the desired reaction temperature. Not only did this serve to clean the char before the gasification test, it also served to drive off any volatile species, yielding a low-heating rate, devolatilized char. Once the test reaction temperature was reached, the test-gas (specified mixtures of CO_2, N_2, and CO) was admitted into the PTGA chamber. Weight loss was monitored at 5 s intervals over a period of 120–1200 min, measured from the start of the heating ramp. Drag and buoyancy effects were taken into account by running a baseline test at each condition with no sample in the sample pan. Subtraction of measurements from runs with and without the sample yields drag- and buoyancy-corrected weight loss data. The corrected PTGA thermograms (weight vs. time curves) were analyzed to determine the char conversion rates as functions of conversion. The conversion rate data were combined with the specific surface area data to determine $R_{i,C}$ as a function of conversion, via Eq. 5.

Arrhenius parameters (A and E) that describe the reaction rate coefficients of reactions (R.1f), (R.1r), (R.4f), and (R.5) were found via a nonlinear least squares scheme in which the differences between measured PTGA thermograms and calculated thermograms were minimized. The calculated thermograms were obtained by integrating the following expression for weight change as a result of adsorption and desorption processes:

$$\frac{dW}{dt} = -16\hat{R}\hat{R}_1 + 28\hat{R}\hat{R}_2 + 12\hat{R}\hat{R}_3 - 28\hat{R}\hat{R}_4 + 16\hat{R}\hat{R}_5 \qquad (12)$$

The coefficients are derived from the difference between the molecular weights of the reactant and product gases for each reaction. Evaluation of the reaction rates requires the simultaneous integration of Eqs. 4–9. The values determined for the pre-exponential factors and activation energies are shown in Table 3. At one atmosphere, the thermograms are relatively insensitive to the rate of reactions (R.3) and (R.4f). Consequently the Arrhenius parameters for these reactions were adjusted to be comparable to that determined for a synthetic char in previous work where tests at high pressures were performed.[13]

Comparisons between predicted and calculated weight loss profiles are shown in Figure 4 for gasification in (a) 100% CO_2 at selected temperatures, (b) selected CO_2/N_2 mixtures at 1173 K, and (c) a 50/50% CO_2/CO mixture at selected temperatures. In agreement with the measurements, the model predicts a weight gain at the onset of gasification, when the weight of oxygen atoms adsorbed on the carbona-

Table 3. Kinetic Parameters Determined for the Activated Carbon

		A_i*	E (kJ/mol)	σ (kJ/mol)
$C_f + CO_2 \rightarrow C(O) + CO$	(R.1f)	5.00*e*03	185	–
$C(O) + CO \rightarrow C_f + CO_2$	(R.1r)	1.08*e*02	89.7	–
$C_b + C(O) \rightarrow CO + C_f$	(R.2)	1.00*e*13	375	28
$C_b + C(O) + CO_2 \rightarrow 2\ CO + C(O)$	(R.3)	1.00*e*04	58	–
$C_f + CO \rightarrow C(CO)$	(R.4f)	0.89	148	–
$C(CO) \rightarrow C_f + CO$	(R.4r)	1.00*e*13	455	53
$CO + C(CO) \rightarrow CO_2 + 2\ C_f$	(R.5)	1.01*e*07	262	–

*$k_i = A_i \exp(E_i/_R T)$, units of A_i are consistent with surface concentrations in mol/m^2-surface, gas-phase concentrations in mol/m^3-fluid, and time in s.

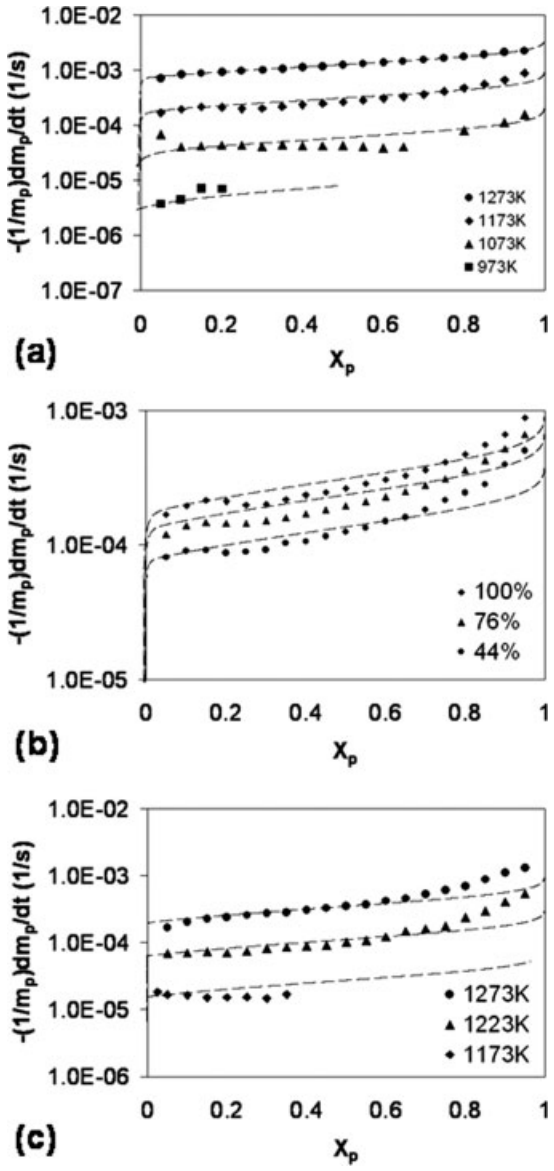

Figure 4. Particle conversion rate as a function of fractional weight loss (x_p) for the activated carbon.

Conditions include (a) 100% CO_2 at 973/1073/1173/1273 K, (b) 100/76/44% CO_2 in N_2 mixtures at 1173 K, and (c) 50% CO/CO_2 at 1173/1223/1273 K.

ceous particle surfaces is greater than the weight of carbon atoms desorbed from the surfaces. This leads to negative values for particle conversion at early times since the weight of the particle at these times is greater than the initial weight of the particle. The agreement depicted is deemed to be satisfactory. A slight under-prediction at high particle conversions is noted; this could possibly be associated with the over-prediction of specific surface area at high conversions. The agreement exhibited serves to validate the reaction mechanism, the kinetic parameters and the surface area parameter determined for the coconut char used in the DCFC experiments.

To assure that tests within the PTGA are within the kinetically limited regime, the Thiele modulus, ϕ_s, of the carbon particles are estimated.[27] The Thiele modulus, given by Eq. 13, provides a quantitative comparison of the relative effects of pore diffusion and chemical reaction within the particle.

$$\phi_s = r_p \sqrt{\frac{\hat{R}_{CO_2} S_{g,C} \rho_p}{[CO_2]_0 \varepsilon_p D_{eff}}} \tag{13}$$

In this formulation, r_p is the mean particle radius, ρ_p/ε_p is the mass of carbon per volume of gas within a particle (g/m^3-fluid), $[CO_2]_0$ is the concentration in the bulk gas phase outside of the particle (mol/m^3), and D_{eff} is the effective pore diffusivity within the particle (m^2/s). For the 100–125 micron diameter activated carbon particles used in this PTGA analysis, the effective pore diffusivity, with the combined effects of Knudsen and continuum diffusion, is estimated to be in the range of 1e-7 to 1e-6 m^2/s in the temperature range of interest. For the conditions tested in the PTGA, the Thiele modulus ranges from 0.05 to 0.6. Values of $\phi_s < 1$ suggest that reactions for the gas species occur under kinetically limited conditions.

The DCFC facility

Our DCFC reactor design consists of a 40-cm long, 2.5-cm diameter tubular quartz reactor that is expanded at the top end to 5 cm to prevent the outflow of carbon particles that could be entrained in the freeboard from lower portions of the reactor. During testing, 16 g of dry, carbonaceous material are added to the reactor, forming a bed of particles about 10 cm in height near the lower end of the reactor. The activated carbon particles have a size range of 75–300 μm, with a mean size of 155 μm as determined by an external surface area weighted average[28] based on scanning electron microscope images. This average particle size, based on sur-

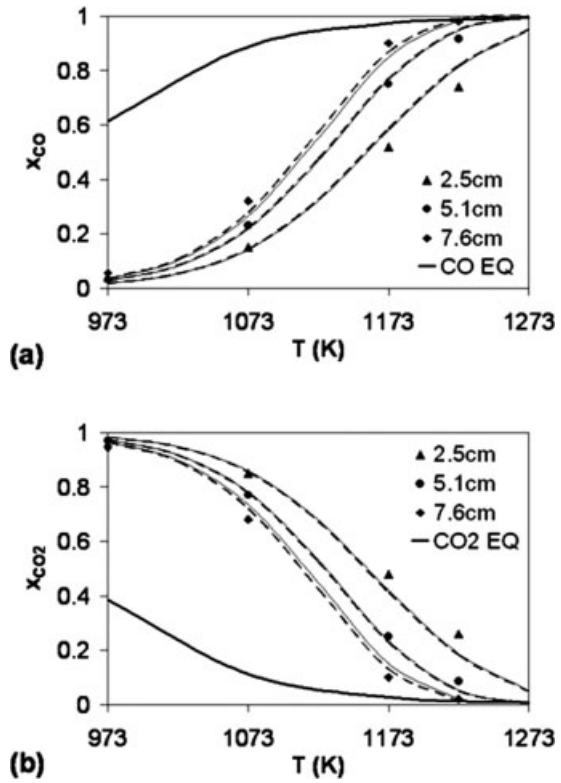

Figure 5. (a) CO and (b) CO_2 mole fractions as a function of temperature at bed heights of 2.5, 5.0, and 7.6 cm.

For comparison, equilibrium values are included for the Boudouard reaction: $C + CO_2 \rightarrow 2CO$.

face area, can then be used to estimate bed properties such as permeability and fluidization velocity.

The preheated fluidizing gas enters the reactor through a port at the bottom of the reactor at the gasification temperature. A tubular furnace placed around the reactor is used to maintain a uniform bed temperature. The temperatures employed in the particle bed fall within the same range as those tested in the PTGA.

During operation, the bed is minimally fluidized using preheated CO_2, with the CO_2 velocity being less than the minimum fluidization velocity for the medium. There is little, but noticeable movement of particles in the bed. Gases leaving the DCFC facility are directed to a gas chromatograph where measurements are made for the CO, CO_2, and O_2 mole fractions in the exhaust. In a series of tests at a selected inlet CO_2 flow rate, incremental amounts of carbon were added to the reactor yielding beds of varying heights. The gases leaving the reactor were monitored for each incremental bed height, yielding information on the CO and CO_2 concentration profile through the bed as a function of height in the bed for the CO_2 flow rate selected. Bed temperature is monitored and controlled with an immersed, 6.4 mm K-type thermocouple, located on the reactor centerline.

The symbols in Figures 5a, b represent the CO and CO_2 mole fractions, respectively, measured at selected bed heights at bed temperatures of 973, 1073, 1173, and 1223 K. To facilitate comparisons, at each bed temperature selected the effluent gas flow rate was maintained at 15 mL/min (at 298 K and 1 atm), as used previously in the experimental DCFC tests.[34] The inlet flow rates ranged from 7.6–14.2 mL/min, as calculated from a steady state oxygen balance. At each selected bed temperature, the CO concentration is noted to increase with increasing height in the bed. Only at the highest bed temperatures, when reaction rates are greatest, are the equilibrium concentrations (the heavy solid curve) approached. The CO_2 profiles exhibit a corresponding decrease with increasing height in the bed. At the highest gas temperature employed, equilibrium values are reached at a bed-height of 7.6 cm. The lines are the results of calculations using the model developed below to characterize the effects of mass transport and chemical reaction in the fluidized bed of particles. The agreement is satisfactory, further validating the reaction mechanism and values determined for the rate parameters and specific surface area parameter. It also validates the approach used in modeling the bed dynamics.

The inlet velocity is in the range of 0.1–0.2 cm/s (maintaining a 15 mL/min effluent flow rate), and the minimum fluidization velocity is estimated to be in the range of 0.05–0.2 cm/s. By observation, the bed is below the bubbling regime (bubbling was observed above about 1.0 cm/s); there is no large-scale movement of the solid particles in the bed although some agitation is observed.

Modeling bed dynamics

A model was developed to describe the effects of mass transport and chemical reaction in a minimally fluidized bed of particles having a fuel cell anode located along the inner boundary of the annular bed where CO oxidation occurs. Carbon dioxide is used as the fluidizing gas. Allowances are made for axial and radial convection, axial and radial diffusion, and chemical reaction in the bed of particles. Finite chemical reaction rates are used to describe the rates of heterogeneous reactions in the bed. A spatially constant current density is specified at the bed boundary adjacent to the fuel cell anode. The fuel cell I-V behavior is not specified here, so no assumptions are made regarding the limiting anode mechanism. At the anode-bed boundary, there is a total flux of CO leaving the particle bed (into the anode) and a total flux of CO_2 entering the particle bed (from the anode). Specification of the current density uniquely determines these fluxes. The model applies only to the particle bed domain, and is used to gauge what current density could be supported by the fuel cell in the carbon bed. The model is adequate for small particles, relative to the reactor length scales, that are totally penetrated by the gases flowing in the bed, that is, for particles experiencing chemical kinetics-limited conversion rates. Note that larger particles, with length scales near 300 μm may have Thiele modulus values near unity or slightly greater at the highest temperature conditions. These particles will still be treated as reacting in the kinetically limited regime. As such, concentration gradients within particles in the bed are neglected and the particles are treated as fully penetrated by the local gas conditions.

In the model, the carbon bed is divided into a number of interconnected volume elements in which the carbon particles are uniformly dispersed. Whereas the carbon particles are

confined to each volume element, the gaseous species are transported between the elements via convection and diffusion.

The gas-phase mass conservation equation is given by Eq. 14, where ρ is the density of the

$$\nabla \cdot (\rho \vec{u}) = \frac{S_{g,C} M_C}{V_{bed}\left(\varepsilon_{bed} + (1-\varepsilon_{bed})\varepsilon_p\right)} \left(\hat{M}_{CO}\hat{R}_{CO} + \hat{M}_{CO_2}\hat{R}_{CO_2}\right) \tag{14}$$

gas, $\bar{u}$ is the superficial convective velocity, M_C is the mass of carbon in the bed, V_{bed} is the geometric volume of the particle bed, ε_{bed} is the bed porosity, and ε_p is particle porosity. Darcy's law,

$$\vec{u} = -(k/\mu)\nabla p \tag{15}$$

where k is the effective bed permeability, μ is the gas viscosity, and p is the pressure, is used to describe the convective velocity distribution through the interstitial space between the particles in the bed.[29] The bed permeability is estimated using the Blake-Kozeny equation[29] which is suitable in the low velocity regime of this study. The bed permeability is based on the mean carbon particle size and the bed porosity. The CO and CO_2 reaction rates are derived from the chemical reaction mechanism, as discussed above (see Eqs. 7 and 8).

Transport of CO and CO_2 through the bed are governed by the following differential equation:

$$\vec{u} \cdot \nabla C_i - \nabla \cdot (D_{eff} \nabla C_i) = \frac{S_{g,C} M_C}{V_{bed}\left(\varepsilon_{bed} + (1-\varepsilon_{bed})\varepsilon_p\right)} \hat{R}_i \tag{16}$$

where the effective mixture diffusivity, D_{eff}, is determined from the binary diffusivities between the gases involved and the bed porosity and tortuosity factor. Binary diffusion coefficients between gas-pairs and the mixture viscosity are calculated based on the Chapman-Enskog theory of gases. Ideal gas behavior is assumed, and the bed is assumed to be isothermal.

Equations 13 and 14, written for the CO and CO_2 concentrations, combined with Eqs. 5, 9, and 10 for the mass of carbon and the adsorbed O and CO concentrations, respectively, constitute the set of coupled differential equations that are solved numerically to determine the convective velocity and the gas-phase and adsorbed-atom concentrations in each volume element of the bed. Quantities such as specific surface area, intrinsic reactivity and carbon conversion fraction at any time are determined algebraically from these variables using the relations already presented. Other dependent quantities that permit the calculation of bed transport properties are also determined via algebraic relations involving these variables.

The boundary conditions for this annular flow system depend on the fluxes at the boundaries. At the inlet ($z = 0$), the CO_2 concentration and inlet velocity are specified from the assigned inflow. At the outlet ($z = L$), the pressure is fixed at 1 atm; both radial and axial diffusive fluxes are assumed to be negligible, convection being the only constraint. The outer bed wall is assumed to be impermeable to all species and hence, all fluxes are set to zero along the outer wall ($r = R_o$). The inner bed wall boundary condition

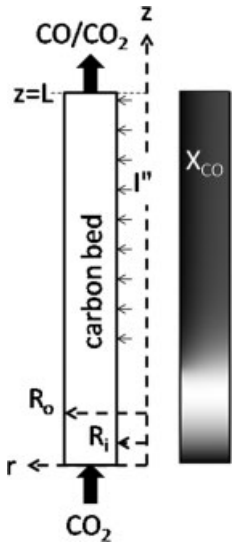

Figure 6. Split view of imbedded anode geometry and typical COMSOL output for CO mole fraction (light corresponds to higher CO mole fractions, dark to lower CO mole fractions).

depends on the configuration modeled. The data modeled in Figure 5 were taken with a thermocouple probe (1.6 mm diameter) on the reactor centerline. The inner radial boundary condition is changed from the insulation constraint of the thermocouple to a specified flux condition to simulate fuel cell conditions. The inner bed radius is also increased from 1.6 mm (thermocouple) to 6.4 mm which is typical of fuel cells used previously. Along the anodic surface, beyond 2.54 cm, the oxygen atom flux is now related to the current density I via the relation $J_o = I/nF$, where $n = 2$. The convective velocity in the radial direction leaving the surface as a consequence of CO oxidation to CO_2 (Stefan flow) is given by

$$u_r(R_i, z) = \left(\frac{I}{nF}\right)\left(\frac{\hat{M}_{CO_2} - \hat{M}_{CO}}{\rho}\right) \tag{17}$$

where ρ is the local gas-phase mixture density at the anode and $\hat{M}_i$ denotes the molecular weight of species i. The 2.54 cm entry region upstream of the anode, without current flux, is similar to that employed in previous studies.[3,4]

The model is implemented using COMSOL, a multiphysics finite element software package. Model output for CO mole fraction is shown in Figure 5, showing good agreement with experimental carbon bed data. The dashed lines correspond to the fixed bed condition, and the thin solid lines correspond to the minimum fluidization condition. The fixed and minimally fluidized configurations give almost identical results, signifying that the effects of bed expansion are not significant for this system. Figure 6 shows a split, mirror view of a typical COMSOL output for CO mole fraction and a schematic showing the imbedded anode configuration.

Results and Discussion

The described model is used to predict the CO and CO_2 concentration profiles established in a fixed bed of particles

for specified current densities, inlet CO_2 flow rates, and bed temperatures. Chemical reaction in the bed is characterized using the reaction mechanism and rate parameters presented in Table 3. Key results are summarized in Figures 7 and 8.

In Figure 7a, the axial CO mole fraction profiles established along the inner wall of the bed when the bed temperature is 1173 K and the inlet CO_2 flow rate is 10 mL/min are shown. At this boundary, CO is consumed (i.e., flows out of the bed) and CO_2 is produced (i.e., flows into the bed). In the entrance region upstream of the anode, the CO builds up due to bed chemistry. At the start of the anodic surface (z = 0.025 m), the effects of current density become observable. Increase in the current density results in increased CO conversion to CO_2. The CO profiles represent the combined effects of CO consumption at the anodic surface and CO production and transport of CO in the bed to the surface. This CO mole fraction along the anodic surface represents a minimum in the radial CO profile at that bed height. At current densities of practical interest, the CO mole fraction at the anode surface at the exit ($z = L$) represents the lowest CO mole fraction along the anode.

At each axial height in the fluidized bed of particles, the CO mole fraction varies in the radial direction owing to CO consumption along the anodic surface. At each height, the radial CO profile decreases slightly as the distance from the outer wall is increased but rapidly decreases as the anode is approached. The curves shown in Figure 7b indicate that the mixed mean CO mole fraction at the bed exit decreases as the current density is increased, a consequence of increased CO consumption relative to CO production. Temperatures below 1123 K are not shown, since the corresponding current densities are below the practical limit due to slow gasification kinetics.

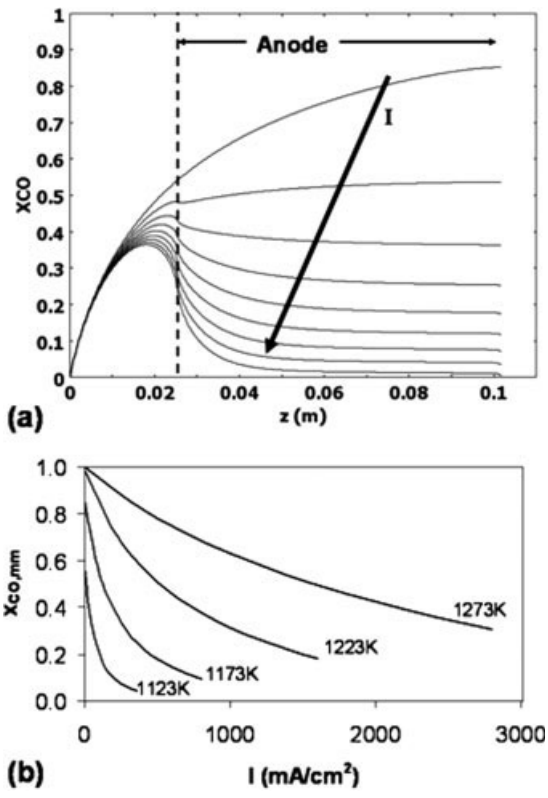

Figure 7. (a) Calculated CO mole fraction at $r = R_i$ at 1173 K for current densities ranging from 0 to 800 mA/cm^2 (in 100 mA/cm^2 intervals). (b) Calculated mixed mean CO mole fractions exiting the carbon bed vs. current density for various temperatures.

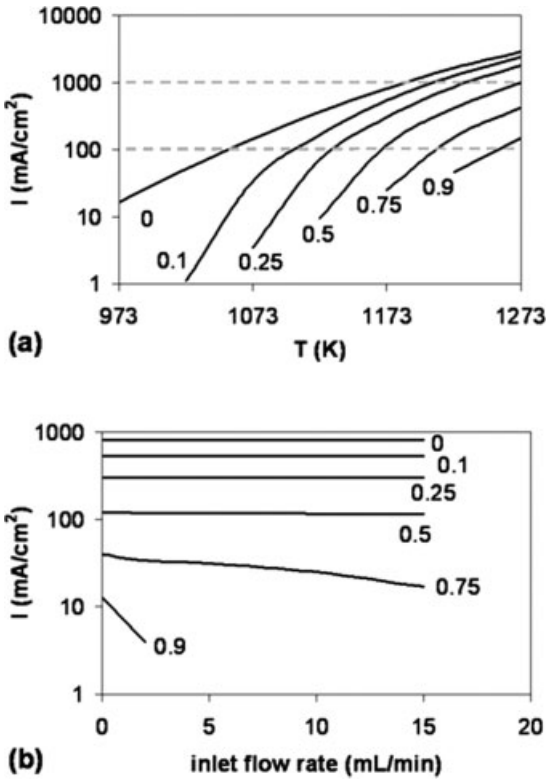

Figure 8. Calculated terminal current density for various terminal CO mole fractions, plotted against (a) bed temperature and (b) inlet CO_2 flow rate.

The current density that produced a given CO mole fraction at the bed exit on the anodic surface is referred to as the terminal current density. This value is a representation of the current density that can be sustained by the carbon bed. In Figure 8a, terminal current densities that yield specified CO mole fractions at the bed exit at the anode are shown, that is, at $r = R_i$ and $z = L$. CO mole fractions at this point in the bed are referred to as terminal CO mole fractions. A terminal CO mole fraction of zero yields the lowest mean CO mole fraction at the bed exit. The terminal current density that yields a terminal CO mole fraction of zero defines an operating limitation. Any higher current density leads to a "starved" anode, there not being sufficient CO to consume the oxygen that diffused across the electrolyte to the anodic TPBs. During practical operation, fuel utilizations of nominally 85% are common to maintain sufficient chemical driving forces. Terminal currents depend on the bed temperature and inlet CO_2 flow rate. The dashed lines in Figure 8a bound the current density window of practical interest. Our model suggests that this fuel cell arrangement is capable of sustaining several hundred milliamps per square centimeter.

The impact of inlet CO_2 flow rate on the terminal current density is shown in Figure 8b for a bed temperature of 1173 K. The model indicates that terminal current density is not a strong function of inlet CO_2 flow rate except at the highest CO terminal levels. In other words, low inlet CO_2 flow rates are required if high CO mole fractions are desired. There is a maximum in terminal current density at zero inlet flow rate for all cases and a monotonic decrease in terminal current density as inlet flow rate is increased. In general, higher bed temperatures further reduce the effect of flow rate, whereas lower bed temperatures show increased sensitivity.

In the case coal or biomass were used as the primary fuel instead of activated carbon, the model would need to be modified to take into account the solid fuel devolatilization products. Among these, sulfur-containing and chlorine-containing species and trace heavy metals may poison and deactivate the anode catalyst, adversely impacting fuel cell performance. On the other hand, the presence of hydrogen is expected to enhance fuel cell performance as a consequence of the higher charge transfer rate at the anode.

Conclusions

A carbon bed model has been developed that describes the effects of mass transport and chemical reaction in the minimally fluidized bed of a direct carbon fuel cell. Kinetic rate parameters used in the model are determined independently for the carbonaceous fuel from thermogravimetric analysis. The Arrhenius parameters extracted from least squares analysis fall within the expected ranges and simulation of carbon bed experiments agree favorably, further validating the kinetic parameters. The model permits the determination of the CO mole fraction in the exit of the DCFC, an important concern for development of direct carbon fuel cell technology. The model supports that there are no fundamental limitations for practical realization of DCFC technology based on carbon gasification. Current densities ranging from 100 to 1000 mA/cm^2 are sustainable in the temperature range of interest. The terminal current density is a strong function of temperature, due to the exponential temperature dependence of the gasification reactions. The CO_2 flow rate does not significantly affect the achievable current density, except at larger terminal CO concentrations. Practical operating constraints, I-V characteristics, and practical fuel reactivities will ultimately determine the achievable current density.

Acknowledgments

Research support for advanced coal research at Stanford University, in the form of an unrestricted gift from Direct Carbon Technologies (DCT), LLC, is greatly appreciated.

Literature Cited

1. Energy Information Administration (EIA). *International Energy Annual 2004*. 2006. Available at: http://www.eia.doe.gov/iea. Accessed March 1, 2008.
2. National Research Council Report. *COAL: Research and Development to Support National Energy Policy*. Washington, DC: National Academy Press, 2007:143.
3. Li S, Lee AC, Mitchell RE, Gür TM. Direct carbon conversion in a helium fluidized bed fuel cell. *Solid State Ionics*. 2007;179:1549–1552.
4. Lee AC, Li S, Mitchell RE, Gür TM. Conversion of solid carbonaceous fuels in a fluidized bed fuel cell. *Electrochem Solid State Lett*. 2008;11:B20–B23.
5. Williams KR. *An Introduction to Fuel Cells*. Amsterdam: Elsevier Publishing Company, 1966.
6. Jacques WW. Electricity direct from coal. *Harper's Magazine*. 1896:94;144–150.
7. Weaver RD, Leach SC, Bayce AE, Nanis L. *Direct Electrochemical Generation of Electricity from Coal*. SRI, Menlo Park, CA 94025, 1979; SAN-0115/105–1.
8. Cherepy NJ, Krueger R, Fiet KJ, Jankowski AJ, Cooper JF. Direct conversion of carbon fuels in a molten carbonate fuel cell. *J Electrochem Soc*. 2005;152:A80–A87.
9. Pesavento PV, inventor; Scientific Applications & Research Associates, Inc., Assignee. Carbon-air fuel cell. U.S. patent 6 200 697, March 13, 2001.
10. Yentekakis IV, Debenedetti PG, Costa B. A novel fused metal anode solid electrolyte fuel cell for direct coal gasification: a steady-state model. *Ind Eng Chem Res*. 1989;28:1414–1424.
11. Gopalan S, Ye G, Pal UB. Regenerative, coal-based solid oxide fuel cell-electrolyzers. *J Power Sources*. 2006;162:74–80.
12. Gür TM, Huggins RA. Direct electrochemical conversion of carbon to electrical energy in a high temperature fuel cell. *J Electrochem Soc*. 1992;139:L95–L97.
13. Ma L. *Combustion and Gasification of Chars in Oxygen and Carbon Dioxide at Elevated Pressure* [Dissertation]. Stanford, CA: Mechanical Engineering Dept., Stanford University, 2006.
14. Ergun S. Kinetics of the reaction of carbon with carbon dioxide. *J Phys Chem*. 1956;60:480–485.
15. Blackwood JD, Ingeme AJ. The reaction of carbon with carbon dioxide at high pressure. *Aust J Chem*. 1960;13:194–209.
16. Koenig PC, Squires RG, Laurendeau NM. Char gasification by carbon dioxide: further evidence for a two-site model. *Fuel*. 1986; 65:412–416.
17. Tsai N. *Influence of High CO Concentration on the CO_2 Gasification of a Selected Coal Char* [Dissertation]. Stanford, CA: Mechanical Engineering Dept., Stanford University, 1998.
18. Du Z, Sarofim AF, Longwell JP. Activation energy distribution in temperature-programmed desorption: modeling and application to the soot oxygen system. *Energy Fuels*. 1990;4:296–302.
19. Du Z, Sarofim AF, Longwell JP, Mims CA. Kinetic measurement and modeling of carbon oxidation. *Energy Fuels*. 1991;5:214–221.
20. Haynes BS, Newbury TG. Oxyreactivity of carbon surface oxides. *Proc Combust Inst*. 2000;28:2197–2203.
21. Haynes BS. A turnover model for carbon reactivity. I. Development. *Combust Flame*. 2001;126:1421–1432.
22. Ma MC, Haynes BS. Surface heterogeneity in the formation and decomposition of carbon surface oxides. *Proc Combust Inst*. 1996;26:3119–3125.
23. Bhatia SK, Perlmutter DD. A random pore model for fluid-solid reactions. I. Isothermal, kinetic control. *AIChE J*. 1980;26:379–386.
24. Campbell PA. *Investigation into the Roles of Surface Oxide Complexes and Their Distributions in the Carbon-Oxygen Heterogeneous Reaction Mechanism [Dissertation]*. Stanford, CA: Mechanical Engineering Dept., Stanford University, 2006.
25. Campbell PA, Mitchell RE. The impact of the distributions of surface-oxides and their migration on characterization of the heterogeneous carbon-oxygen reaction. *Comb Flame*. 2008;154:47–66.
26. Greg SJ, Sing KSW. *Adsorption, Surface Area and Porosity*, 2nd ed. New York: Academic Press, 1982.
27. Satterfield C. *Mass Transfer in Heterogeneous Catalysis*. MA: The Colonial Press, 1970.
28. Kunii D, Levenspiel O. *Fluidization Engineering*. New York: Wiley, 1969.
29. Bird RB, Stewart WE, Lightfoot EN. *Transport Phenomena*. New York: Wiley, 1960.

Manuscript received Apr. 18, 2008, and revision received Sept. 4, 2008.